

# Dynamic exchange-correlation potentials for the electron gas in dimensionality $D = 3$ and $D = 2$

R. Nifosi, S. Conti,\* and M. P. Tosi

*Istituto Nazionale di Fisica della Materia and Classe di Scienze, Scuola Normale Superiore, I-56126 Pisa, Italy*  
(February 1, 2008)

Recent progress in the formulation of a fully dynamical local approximation to time-dependent Density Functional Theory appeals to the longitudinal and transverse components of the exchange and correlation kernel in the linear current-density response of the homogeneous fluid at long wavelength. Both components are evaluated for the electron gas in dimensionality  $D = 3$  and  $D = 2$  by an approximate decoupling in the equation of motion for the current density, which accounts for processes of excitation of two electron-hole pairs. Each pair is treated in the random phase approximation, but the role of exchange and correlation is also examined; in addition, final-state exchange processes are included phenomenologically so as to satisfy the exactly known high-frequency behaviours of the kernel. The transverse and longitudinal spectra involve the same decay channels and are similar in shape. A two-plasmon threshold in the spectrum for two-pair excitations in  $D = 3$  leads to a sharp minimum in the real part of the exchange and correlation kernel at twice the plasma frequency. In  $D = 2$  the same mechanism leads to a broad spectral peak and to a broad minimum in the real part of the kernel, as a consequence of the dispersion law of the plasmon vanishing at long wavelength. The numerical results have been fitted to simple analytic functions.

71.45Gm

## I. INTRODUCTION

The plasmon dispersion relation and the dynamic structure factor of the conduction electrons in simple metals are known from Electron Energy Loss and Inelastic X-ray Scattering experiments.<sup>1,2</sup> Both electron-gas correlations and band structure enter in determining these properties and Time-Dependent (TD) Density Functional Theory (DFT) provides a general framework which can account for both. The generality of the DFT method<sup>3,4</sup> in dealing with inhomogeneous electron systems motivates interest in the derivation of sensible approximations to the dynamic exchange and correlation (xc) potential, beyond the adiabatic regime<sup>5–8</sup> whose applicability is limited to low-frequency phenomena.

A local density approximation for a scalar xc potential in time-dependent phenomena was proposed in early work of Gross and Kohn.<sup>9,10</sup> However, detailed analysis of the constraints coming from basic conservation laws has shown that inconsistencies can arise and are associated with the non-existence of a gradient expansion for the frequency-dependent xc potential in terms of the density alone.<sup>4,11–14</sup> Recently Vignale and Kohn<sup>15,16</sup> have overcome these difficulties by resorting to a dynamic xc *vector* potential even in the case of an inhomogeneous system subject to an external *scalar* potential. They obtained an explicit local-density expression for the xc vector potential in the linear response regime in terms of correlations of longitudinal and transverse currents in the homogeneous electron gas. This expression becomes exact when the equilibrium electron density and the external potential are slowly varying in space, on length scales set by  $k_F^{-1}$  and  $v_F/\omega$  where  $k_F$  and  $v_F$  are the local Fermi wave-number and velocity.

The results of Vignale and Kohn have been interpreted in terms of complex, frequency-dependent viscoelastic coefficients, allowing a non-linear generalization up to second order in the spatial gradients.<sup>17</sup> Within this framework, Ullrich and Vignale<sup>18</sup> have developed a simple computational scheme for the calculation of the linewidths of non-Landau-damped collective excitations, whose decay is solely due to dynamical xc effects. The order-of-magnitude enhancement over the homogeneous-gas approximation reported in the application to quantum strips<sup>18</sup> emphasizes the relevance of the interplay between inhomogeneity and dynamical xc effects.

The work of Vignale and Kohn has brought new interest to the evaluation of the longitudinal and transverse components of the dynamic xc kernel [ $f_{xc}^L(\omega)$  and  $f_{xc}^T(\omega)$ , say] in the homogeneous electron gas at long wavelength. An interpolation between the known asymptotic behaviours at low and high frequency was proposed for the longitudinal component by Gross and Kohn<sup>9,10</sup> and later extended to finite wave number by Dabrowski.<sup>19</sup> It was subsequently noticed<sup>20</sup> that the long-wavelength longitudinal spectrum is closely related to processes of excitation of two correlated electron-hole pairs in the electron gas. These have been studied by perturbative methods in the early work of Dubois<sup>21,22</sup> and by several other authors.<sup>23–29</sup> The inclusion of dynamic screening in the Random Phase Approximation (RPA) leads to a mode-coupling form of the spectrum<sup>24</sup> and inclusion of final-state exchange processes is needed to recover the exact high-frequency behaviour calculated by Glick and Long.<sup>25</sup> A similar expression has been more recently obtained by Neilson *et al.*<sup>30</sup> within a memory function formalism for the electron gas in dimensionality  $D = 2$ .

With regard to the transverse component of the long-

wavelength xc kernel  $f_{xc}^T(\omega)$ , Vignale and Kohn<sup>15,16</sup> have given a first-order perturbative estimate and obtained the high-frequency limit. We have subsequently briefly reported on the results of a full calculation of  $f_{xc}^T(\omega)$  for the electron gas in three spatial dimensions,<sup>31</sup> and on preliminary results in the two-dimensional case.<sup>32</sup> These calculations were based on the two-pair model treated in the RPA and corrected for final-state exchange processes (hereafter indicated as RPAs).

In the present work we give a full account of our approach to the evaluation of the dynamic xc kernels  $f_{xc}^L(\omega)$  and  $f_{xc}^T(\omega)$ , including an exact expression for  $f_{xc}^{L,T}(\omega)$  in terms of four-point response functions. We also extend our calculations to (i) fully evaluate the dynamic xc kernels for the electron gas with  $e^2/r$  interactions in  $D = 2$ , and (ii) examine the role of including exchange and correlation in the screening processes entering the RPAs.

The lay-out of the paper is as follows. Section II presents the theory underlying our calculations, with the help of three Appendices. We start from the definition of  $f_{xc}^{L,T}(\omega)$  in terms of the current-current response functions for the ideal and the real electron gas and proceed to evaluate the ideal-gas response at high frequency and to derive an exact expression for the real-gas response in terms of a four-point response function. An approximate decoupling of this latter function into products of two-point response functions introduces the two-pair approximation. Screening at the RPA level or better and phenomenological inclusion of final-state exchange finally lead to the formulae used in our calculations. The numerical results are presented in Section III together with fits to analytic functions incorporating the known asymptotic behaviours and aimed at facilitating numerical applications within the time-dependent DFT formalism. The role of exchange and correlation in the treatment of each pair is studied in Section IV. We conclude with a brief summary in Section V.

## II. THEORY: EXACT RESULTS AND TWO-PAIR MODEL

The longitudinal (L) and transverse (T) kernels  $f_{xc}^{L,T}(\omega)$  of the homogeneous electron gas are defined as the  $k \rightarrow 0$  limit of the functions

$$f_{xc}^{L,T}(k, \omega) = \frac{\omega^2}{k^2} \left[ \frac{1}{\chi_{L,T}^0(k, \omega) + n/m} - \frac{1}{\chi_{L,T}(k, \omega) + n/m} \right] - v_k^{L,T}. \quad (1)$$

Here,  $\chi_{L(T)}$  is the longitudinal (transverse) current-current response function of the homogeneous fluid at density  $n$ ,  $\chi_{L(T)}^0$  is the corresponding ideal-gas response function,  $v_k^L$  is the Coulomb potential ( $v_k^L = 4\pi e^2/k^2$  in  $D = 3$  and  $v_k^L = 2\pi e^2/k$  in  $D = 2$ ) and  $v_k^T = 0$ . We

remark<sup>33,34</sup> that  $\chi_L(k, \omega)$  is related to the density-density response function  $\chi(k, \omega)$  by

$$\chi_L(k, \omega) + \frac{n}{m} = \frac{\omega^2}{k^2} \chi(k, \omega) \quad (2)$$

and that  $f_{xc}^L$  is proportional to the local field factor  $G(k, \omega)$  entering the dielectric function of the electron gas, according to  $f_{xc}^L(k, \omega) = -v_k^L G(k, \omega)$ .

The longitudinal response function  $\chi_L^0(k, \omega)$  is immediately obtained from the Lindhard susceptibility<sup>33–35</sup> in  $D = 3$  and from the Stern susceptibility<sup>36</sup> in  $D = 2$  by using (2) for the ideal Fermi gas. The calculation of  $\chi_T^0(k, \omega)$  for the ideal Fermi gas in  $D = 3$  and  $D = 2$  is reported in Appendix A.

Equation (1) may be written in terms of the proper current response functions  $\tilde{\chi}_{L,T}(k, \omega)$ ,

$$f_{xc}^{L,T}(k, \omega) = \frac{\omega^2}{k^2} \left[ \frac{1}{\chi_{L,T}^0(k, \omega) + n/m} - \frac{1}{\tilde{\chi}_{L,T}(k, \omega) + n/m} \right]. \quad (3)$$

This emphasizes that the plasmon does not contribute to  $f_{xc}^L(k, \omega)$ , leaving only contributions from multi-pair excitations in the limit  $k \rightarrow 0$ . In fact, to leading order in the long wavelength limit we have from (3)

$$\text{Im} f_{xc}^{L,T}(\omega) = \lim_{k \rightarrow 0} \frac{m^2 \omega^2}{n^2 k^2} \text{Im} \tilde{\chi}_{L,T}(k, \omega). \quad (4)$$

We proceed below to evaluate the imaginary part of the kernels, from which their real part will be obtained by means of the Kramers-Kronig relation. The equation of motion for  $\chi_{ij}(\mathbf{k}, \omega)$  can be obtained from the definition of a general response function in terms of unequal-time commutators,

$$\langle\langle A; B \rangle\rangle_\omega = -i \int_0^\infty e^{i(\omega+i\epsilon)t} \langle [A(t), B(0)] \rangle dt \quad (5)$$

where  $A(t) = e^{iHt} A e^{-iHt}$ ,  $\langle \dots \rangle$  denotes a ground-state expectation value, and  $\epsilon$  is a positive infinitesimal. The current-current response  $\chi_{ij}(\mathbf{k}, \omega) = \langle\langle \mathbf{j}_\mathbf{k}^i; \mathbf{j}_{-\mathbf{k}}^j \rangle\rangle_\omega$  satisfies the equation of motion

$$\omega^2 \chi_{ij}(\mathbf{k}, \omega) = \left\langle \left[ [\mathbf{j}_\mathbf{k}^i, H], \mathbf{j}_{-\mathbf{k}}^j \right] \right\rangle - \left\langle \left\langle [\mathbf{j}_\mathbf{k}^i, H]; [\mathbf{j}_{-\mathbf{k}}^j, H] \right\rangle \right\rangle_\omega \quad (6)$$

where the first term is real and independent of  $\omega$ . It will be evaluated below in the discussion of the real part of  $f_{xc}$  (Eqs. 15–17). Quite lengthy calculations, which are briefly reported in Appendix B, lead to the long-wavelength result

$$\begin{aligned} \text{Im} \tilde{\chi}_{ij}(\mathbf{k}, \omega) &= \frac{1}{m^2 V^2 \omega^4} \sum_{\mathbf{q}, \mathbf{q}'} \text{Im} \left\langle \left\langle \mathbf{j}_\mathbf{q}^i \rho_{-\mathbf{q}}; \mathbf{j}_{\mathbf{q}'}^{i'} \rho_{-\mathbf{q}'} \right\rangle \right\rangle_\omega \\ &\times \Gamma^{il}(\mathbf{q}, \mathbf{k}) \Gamma^{jl'}(\mathbf{q}', -\mathbf{k}) + o(k^2) \end{aligned} \quad (7)$$

where the coefficients  $\Gamma^{il}(\mathbf{q}, \mathbf{k})$  are defined in Eq. (B7) and summation over repeated indices is understood. This expression, together with (4), gives an exact result for  $\mathbf{Im}f_{xc}^{L,T}(\omega)$ .

We now discuss some approximate evaluations of Eq. (7). Use of the ideal-gas four-point response function in the RHS gives the exact second-order perturbative value for  $f_{xc}^{L,T}(\omega)$ , which is expected to be accurate at high frequency (see App. C). In Appendix C we derive in this way the leading high-frequency behaviour of the kernel,

$$f_{xc}^{L,T}(\omega) = -a_{L,T}\pi^2 \left(\frac{2}{\pi}\right)^{D-2} \left(\frac{2Ry}{\omega}\right)^{D/2} a_B^D Ry \quad (8)$$

where  $a_B$  is the Bohr radius,  $a_L = 23/30$  and  $a_T = 8/15$  in  $D = 3$ , while  $a_L = 11/16$  and  $a_T = 9/16$  in  $D = 2$ . The longitudinal component of this result was obtained by Glick and Long<sup>25</sup> in  $D = 3$  and by Holas and Singwi<sup>37</sup> in  $D = 2$ . In the low-frequency limit instead, perturbation theory gives an artificial divergence in  $\mathbf{Re}f_{xc}$  and a discontinuity in  $\mathbf{Im}f_{xc}$ , and will not be pursued further.

We obtain an approximate nonperturbative evaluation of (7) by decoupling its RHS within an RPA-like scheme, which in the frequency domain gives

$$\begin{aligned} \mathbf{Im} \langle\langle AB; CD \rangle\rangle_\omega &\simeq - \int_0^\omega \frac{d\omega'}{\pi} [\mathbf{Im} \langle\langle A; C \rangle\rangle_{\omega'} \\ &\times \mathbf{Im} \langle\langle B; D \rangle\rangle_{\omega-\omega'} + \mathbf{Im} \langle\langle A; D \rangle\rangle_{\omega'} \mathbf{Im} \langle\langle B; C \rangle\rangle_{\omega-\omega'}] . \end{aligned} \quad (9)$$

The functions in the RHS of Eq. (9) are understood to be exact response functions of the interacting electron gas. This scheme clearly neglects exchange processes in the final state, which are known to reduce the spectral strength by a factor of 2 at high frequency in perturbative treatments (see Appendix C), but are ineffective at low frequency. This can be physically understood as follows. A two-pair excitation at long wavelength involves the creation of holes with momenta  $\mathbf{p}$  and  $\mathbf{p}'$  inside the Fermi sphere and of electrons with momenta  $\mathbf{p} + \mathbf{q}$  and  $\mathbf{p}' - \mathbf{q}$  outside the Fermi sphere. If the excitation energy  $\omega$  is small compared to the Fermi energy  $\varepsilon_F$ , then necessarily  $|\mathbf{q}| \ll k_F$  and, since on average  $|\mathbf{p} - \mathbf{p}'| \simeq k_F$ , each electron is substantially closer (in  $\mathbf{k}$ -space) to “its” hole than to the other one: exchange processes are thus suppressed in this case (see Fig. 1.a) by a factor  $v_{k_F}^L/v_q^L$  which vanishes for  $q \rightarrow 0$  (i.e.  $\omega \rightarrow 0$ ).<sup>38</sup> Conversely if  $\omega \gg \varepsilon_F$  one has  $|\mathbf{q}| \gg k_F$  and therefore for parallel spins the strengths of direct and exchange processes are equal and opposite (see Fig. 1.b).

On the basis of the above argument, which can be made quantitative at a perturbative level, we phenomenologically incorporate exchange effects by inclusion of a factor

$$g_x(\omega) = \frac{1 + 0.5\omega/2\varepsilon_F}{1 + \omega/2\varepsilon_F}, \quad (10)$$

which interpolates between 1 at low  $\omega$  and 0.5 at high  $\omega$  on the energy scale ( $2\varepsilon_F$ ) of exchange processes. Our

final expression for the imaginary part of the kernel thus is

$$\begin{aligned} \mathbf{Im}f_{xc}^{L,T}(\omega) &= -g_x(\omega) \int_0^\omega \frac{d\omega'}{\pi} \int \frac{d^D q}{(2\pi)^D n^2} (v_q^L)^2 \\ &\times \left[ a_{L,T} \frac{q^2}{\omega'^2} \mathbf{Im}\chi_L(q, \omega') + b_{L,T} \frac{q^2}{\omega^2} \mathbf{Im}\chi_T(q, \omega') \right] \\ &\times \frac{q^2}{(\omega - \omega')^2} \mathbf{Im}\chi_L(q, \omega - \omega'), \end{aligned} \quad (11)$$

with  $a_{L,T}$  as defined below Eq. (8),  $b_L = 8/15$  and  $b_T = 2/5$  in  $D = 3$  and  $b_L = b_T = 1/2$  in  $D = 2$ . The expression for the longitudinal component is equivalent to that obtained in 3D by Hasegawa and Watabe<sup>24</sup> by diagrammatic means and similar to that derived in 2D by Neilson *et al.*<sup>30</sup> (see the discussion in Ref. 20). This result can be physically understood as representing the spectral density of two-pair excitations, which are present at any frequency in the long-wavelength region of the spectrum and provide a mechanism for the decay of the plasmon outside of the single-pair continuum. The resulting linewidth is  $\Gamma_k/\omega_k = -\mathbf{Im}f_{xc}^L(\omega_k)/v_k^L$ .

Considering the low-frequency behaviour of  $\mathbf{Im}\chi_{L,T}(k, \omega)$  it can be shown that at low  $\omega$  Eq. (11) is linear in  $\omega$ , and that to this order the first term in the square brackets does not contribute. The coefficients of this linear behaviour are related<sup>17</sup> to the bulk and shear viscosities of the electron gas,  $\zeta$  and  $\eta$  respectively, via

$$\zeta = -n^2 \lim_{\omega \rightarrow 0} \left[ \frac{\mathbf{Im}f_{xc}^L(\omega)}{\omega} - 2 \frac{D-1}{D} \frac{\mathbf{Im}f_{xc}^T(\omega)}{\omega} \right] \quad (12)$$

and

$$\eta = -n^2 \lim_{\omega \rightarrow 0} \frac{\mathbf{Im}f_{xc}^T(\omega)}{\omega}. \quad (13)$$

The significance of  $\zeta$  and  $\eta$  is the same as in classical hydrodynamics.<sup>39</sup> Both viscosities vanish in the ideal Fermi gas, as well as in the RPA and in static-local-field approximations to the interacting electron gas. Since  $b_L/b_T = 2(D-1)/D$ , also within the present model the bulk viscosity  $\zeta$  vanishes identically. Numerical results for the shear viscosity  $\eta$  will be given below.

We now discuss the real part of the kernels  $f_{xc}^{L,T}(\omega)$ . Once the imaginary part has been evaluated, the real one can be obtained by means of the Kramers-Kronig relation

$$\mathbf{Re}f_{xc}^{L,T}(\omega) = f_{xc}^{L,T}(\infty) + \frac{1}{\pi} \int_{-\infty}^{+\infty} d\omega' \frac{\mathbf{Im}f_{xc}^{L,T}(\omega')}{\omega' - \omega}, \quad (14)$$

where  $f_{xc}^{L,T}(\infty)$  denotes the (real) high-frequency limit of the kernels. This quantity corresponds to the long-wavelength value of the leading spectral moment beyond the  $f$ -sum rule,<sup>33,34</sup> which is the first term on the RHS of Eq. (6). With the definition  $\tilde{M}_{L,T}(k) = \lim_{\omega \rightarrow \infty} \omega^2 \tilde{\chi}_{L,T}(k, \omega)$ , we have

$$\tilde{M}_L(k) = \frac{nk^2}{2m^2} \left[ \frac{k^2}{2m} + \frac{12}{D} \langle ke \rangle + \frac{2}{n} \sum_{\mathbf{q}} v_k^L \frac{(\mathbf{k} \cdot \mathbf{q})^2}{k^4} (S(|\mathbf{q} + \mathbf{k}|) - S(q)) \right], \quad (15)$$

and

$$\tilde{M}_T(k) = \frac{nk^2}{2m^2} \left[ \frac{4}{D} \langle ke \rangle + \frac{1}{n} \sum_{\mathbf{q}} v_k^L \left[ \frac{q^2}{k^2} - \frac{(\mathbf{k} \cdot \mathbf{q})^2}{k^4} \right] (S(|\mathbf{q} + \mathbf{k}|) - S(q)) \right] \quad (16)$$

where  $S(q)$  is the static structure factor and  $\langle ke \rangle$  denotes the true kinetic energy per particle. Expansion at long wavelengths gives the required high- $\omega$  limit of  $f_{xc}^{L,T}(\omega)$ ,

$$f_{xc}^{L,T}(\infty) = \frac{1}{2n} \left[ d_{L,T} (\langle ke \rangle - \langle ke \rangle^0) + e_{L,T} \langle pe \rangle \right] \quad (17)$$

with  $d_L = 4$ ,  $d_T = 4/3$ ,  $e_L = 8/15$  and  $e_T = -4/15$  in  $D = 3$ , and  $d_L = 6$ ,  $d_T = 2$ ,  $e_L = 5/4$  and  $e_T = -1/4$  in  $D = 2$ . The average kinetic and potential energies  $\langle ke \rangle$  and  $\langle pe \rangle$  can be obtained from the Monte Carlo equation of state,<sup>40–42</sup> and  $\langle ke \rangle^0$  denotes the ideal-gas value. The resulting values of  $f_{xc}^{L,T}(\infty)$ , given in Table I ( $D = 3$ ) and Table II ( $D = 2$ ), allow to evaluate numerically Eq. (14) and to obtain the real part of the kernels at any frequency.

The low-frequency limit of  $f_{xc}^{L,T}(\omega)$  is related<sup>17</sup> to the elastic moduli  $K$  and  $\mu$  via

$$K_{xc} = n^2 \left[ f_{xc}^L(0) - 2 \frac{D-1}{D} f_{xc}^T(0) \right] \quad (18)$$

and

$$\mu_{xc} = n^2 f_{xc}^T(0). \quad (19)$$

The significance of  $K$  and  $\mu$  is the same as in classical elasticity,<sup>43</sup> and as usual the suffix  $xc$  indicates that the ideal-gas contribution has been subtracted. Our results for  $K_{xc}$  are in good agreement with the accurate values obtained from the Monte Carlo  $xc$  energy per particle<sup>40–42</sup>  $\epsilon_{xc}^{\text{MC}}(n)$  via  $K_{xc}^{\text{MC}} = n^2 d^2 \epsilon_{xc}^{\text{MC}} / dn^2$  (see below<sup>44</sup>). We finally note that  $K_{xc}$  is also related to the long-wavelength limit of the *static*  $f_{xc}^L(k, 0)$  via the compressibility sum rule,<sup>33</sup>

$$K_{xc} = n^2 \lim_{k \rightarrow 0} \lim_{\omega \rightarrow 0} f_{xc}^L(k, \omega). \quad (20)$$

### III. NUMERICAL RESULTS WITHIN THE RPA

This Section presents results that we have obtained for  $f_{xc}$  from numerical integration of Eqs. (11) and (14) using RPA response functions, which are given by

$$\frac{1}{\chi_{L,T}^{\text{RPA}}(k, \omega) + n/m} = \frac{1}{\chi_{L,T}^0(k, \omega) + n/m} - \frac{k^2}{\omega^2} v_k^{L,T}. \quad (21)$$

In the high-frequency limit the first term in the square brackets of Eq.(11) dominates over the second one, implying  $\text{Im}f_{xc}^T = (a_T/a_L)\text{Im}f_{xc}^L$ ; conversely, for low  $\omega$  the first term is negligible and  $\text{Im}f_{xc}^T = (b_T/b_L)\text{Im}f_{xc}^L$ . Indeed the longitudinal and transverse spectra are very similar, and the transverse one is rather accurately reproduced at all frequencies by setting  $\text{Im}f_{xc}^T(\omega) \simeq 0.72 \cdot \text{Im}f_{xc}^L(\omega)$  in 3D and  $\text{Im}f_{xc}^T(\omega) \simeq 0.85 \cdot \text{Im}f_{xc}^L(\omega)$  in 2D, the proportionality factor being close both to  $a_T/a_L$  and to  $b_T/b_L$ . For the real part of the kernels there is an additional shift due to the different values for  $\omega = \infty$ .

Figure 2 reports the results for the imaginary part of  $f_{xc}^{L,T}$  in 3D at  $r_s = 3$  as functions of  $\omega/\omega_{pl}$  [in 3D  $r_s$  is defined as  $(4\pi n a_B^3/3)^{-1/3}$  and the plasma frequency  $\omega_{pl}$  as  $(4\pi e^2 n/m)^{1/2}$ ]. Both our results and the Gross-Kohn (GK) interpolation<sup>9,10</sup> for  $\text{Im}f_{xc}^{L,T}$  reproduce the high frequency behaviour given by Eq. (8) and are linear at low frequency. As already remarked the bulk viscosity  $\zeta$  vanishes identically within the present model, but the shear viscosity  $\eta$  is finite; numerical results for the latter are given in Table I. From Fig. 2 one can see that our estimate for  $\eta$  is significantly smaller than that of GK. In the intermediate frequency region our curves exhibit a sharp threshold at twice the plasma frequency, which is due to the onset of two-plasmon processes. This is the most remarkable difference from the GK interpolation.

The corresponding real parts of the kernels are shown in Fig. 3. The two-plasmon threshold in the spectrum generates a pronounced minimum at  $\omega = 2\omega_{pl}$  in the real part, which is absent in the smooth GK interpolation. The  $f_{xc}^L(0)$  value was obtained by GK assuming  $f_{xc}^L(0) = K_{xc}/n^2$ , i.e.  $f_{xc}^L(0) = \mu_{xc} = 0$  [see Eqs. (18–19)]; our curves instead are consistent with Eq. (18) with a nonvanishing  $f_{xc}^L(0)$ . Table I reports our results for the elastic moduli  $K_{xc}$  and  $\mu_{xc}$ , obtained from  $\text{Re}f_{xc}$  via Eqs. (18–19). They cannot be expected to be very precise, being obtained through integration over the entire spectrum. With this *caveat*, we note that our numerical estimates for  $K_{xc}$  agree with the accurate Monte Carlo results  $K_{xc}^{\text{MC}}$ , also given in the same Table, within 5%. We note that the  $xc$  contribution to the shear modulus  $\mu_{xc}$  becomes negative at low density; the total shear modulus  $\mu = \mu_{xc} + \frac{2}{5}n\varepsilon_F$ , however, remains positive.

In order to facilitate use of these data in practical TD-DFT computations, an analytical fit has been given in Ref. 31. The constraint  $f_{xc}^L(0) = K_{xc}/n^2$ , which was imposed in the fits following GK, can be removed simply by setting  $\beta = 1$ .

We now turn to the two-dimensional system. Figures 4 and 5 report our results for the imaginary and real parts of  $f_{xc}^{L,T}$  at  $r_s = 3$  [in 2D  $r_s$  is defined as  $(\pi n a_B^2)^{-1/2}$ ]. The main difference with respect to the 3D results is the absence of the sharp two-plasmon threshold in the two-pair excitation spectrum (i.e. in  $\text{Im}f_{xc}$ ), due to the fact that the plasmon dispersion relation vanishes in 2D at

long wavelength. Correspondingly the minimum in the real part of the kernel is much broader. The figures also compare our result for  $f_{xc}^L$  with the interpolation scheme of Holas and Singwi (HS),<sup>37</sup> which is the 2D extension of the GK interpolation. Both curves reproduce the asymptotic limit (17) as well as the high-frequency behaviour of Eq. (8), and both imaginary parts are linear in  $\omega$  at low frequency. Also in the 2D case the minimum in the real part is absent in the GK/HS interpolation scheme.

Table II reports the resulting values of the shear viscosity  $\eta$  and of the elastic moduli  $K_{xc}$  and  $\mu_{xc}$ , obtained as in the 3D case. In 2D the agreement between the bulk modulus  $K_{xc}$  obtained from our data on  $f_{xc}^{L,T}$  and the Monte Carlo value  $K_{xc}^{MC}$  is not as good as in 3D, but still better than 10% at all values of  $r_s$  that we have considered. In contrast to 3D, at low density the total shear modulus  $\mu = \mu_{xc} + \frac{1}{2}n\varepsilon_F$ , turns out to be negative. However, the observed disagreement between  $K_{xc}$  and  $K_{xc}^{MC}$  prevents us from drawing a conclusion about the presence of an instability.

To facilitate application of these results in actual TD-DFT computations, such as the one of Ref. 18, we provide below a simple analytical interpolation. The imaginary part is reproduced by

$$\text{Im}f_{xc}^L(\omega) = -g_x(\omega) \frac{c_1\omega + c_2\omega^2 + c_3\omega^3 + 2c_{HS}\omega^5}{c_0 + c_4\omega^4 + \omega^6} \quad (22)$$

where  $\omega$  is in  $Ry$ ,  $f_{xc}$  in units of  $Ry/n$  and  $c_{HS} = 11\pi/8r_s^2$  is the coefficient of the leading high-frequency behaviour from Eq. (8). The remaining parameters, which we obtained by a least-squares fit to the numerical calculation, are reported in Table III; the transverse component can be approximated by  $\text{Im}f_{xc}^T = 0.85 \text{Im}f_{xc}^L$ . The quality of a typical fit is shown in Figures 4 and 5. Values at intermediate  $r_s$  are best obtained by interpolation of  $f_{xc}(\omega)$  at the same  $\omega$  (in  $Ry$ ); for  $r_s \geq 3$  also the simpler scheme of interpolating the fitted coefficients  $c_0, \dots, c_4$  is viable. The real part can be obtained from Eq. (14), which in this case can be integrated analytically; the resulting expression is quite long and we do not report it.

#### IV. EXCHANGE-CORRELATION EFFECTS ON $f_{xc}$

This Section is aimed at assessing the validity of the results presented above. In the first part we study the effect of correlation in the treatment of each pair, adopting more refined response functions in the RHS of Eq. (11); in the final part we discuss corrections which go beyond the present two-pair model.

We have introduced the effect of correlation in the treatment of each pair in Eq. (11) by means of two of the most successful static-local-field approximations, the Singwi-Tosi-Land-Sjölander<sup>45</sup> (STLS) and the Vashishta-Singwi<sup>46</sup> (VS). In the 3D case, both schemes predict negative plasmon dispersion at large  $r_s$  ( $r_s \geq 5$  in STLS and

$r_s \geq 9$  in VS), in qualitative agreement with experiment.<sup>1</sup> The VS scheme embodies the compressibility sum rule on the static response, and is therefore more reliable in the study of static phenomena. Since these schemes only involve longitudinal currents, the transverse response function is still evaluated at an RPA level.

Figures 6 and 7 compare the RPA results in 3D with those obtained with STLS and VS. At  $r_s = 1$  correlation only gives minor corrections, but at larger  $r_s$  it leads to a divergence, caused by the appearance of negative plasmon dispersion. Figure 8 compares the results obtained with STLS at various densities. The minimum at intermediate frequency gets more pronounced with increasing  $r_s$ , and for  $r_s \geq 5$  becomes a divergence of the form  $\theta(\omega - 2\omega_{min})(\omega - 2\omega_{min})^{-1/2}$ , where  $\omega_{min}$  is the minimum energy of the collective mode.

Introduction of the local field correction significantly increases the shear viscosity  $\eta$ , and leads to large negative values of the shear modulus  $\mu_{xc}$  (e.g. with VS we get  $\mu_{xc} = -0.03$  at  $r_s = 5$  and  $\mu_{xc} = -0.1$  at  $r_s = 10$ , in units of  $2\omega_{pl}n$ ). The relation  $K_{xc} = K_{xc}^{MC}$  is satisfied with the same accuracy as in the RPA case.

Figure 9 displays the dynamical structure factor  $S(k, \omega) = -(2k^2/n\omega^2)\text{Im}\chi_L(k, \omega)$  which is relevant to inelastic scattering experiments. The threshold behaviour at frequency  $2\omega_{pl}$  is a clear-cut signature of the present results for  $f_{xc}$ . The more pronounced singularity present in the STLS curves originates from the negative plasmon dispersion.

We also investigated the role of exchange and correlation in 2D, using the STLS model as generalized in 2D by Jonson.<sup>47</sup> The qualitative behaviour turns out to be similar. Figure 10 reports our results for the imaginary part of  $f_{xc}$  as obtained from RPA and STLS calculations. As in 3D, in STLS the plasmon energy at intermediate wavevector is lower than in RPA, and correspondingly we note a significant increase in the depth of the minimum at intermediate frequency in  $\text{Im}f_{xc}$ . This increase, unlike the 3D case, is significant also at rather high density (see the inset) as a consequence of the enhancement of correlation effects in 2D systems. On the other hand, in 2D no divergence appears in the two-pair spectrum, since no minimum at finite  $k$  is present in the plasmon dispersion. The same is true for the corresponding real parts, which are shown in Fig. 11.

Having discussed at length the role of two-pair processes in the long-wavelength spectrum of the uniform electron gas, we now turn to a qualitative discussion of other effects which have been neglected in the present treatment. Whereas a detailed quantitative calculation is cumbersome, the qualitative role of multi-pair processes beyond two-pairs can be easily grasped by straightforward extension of the present treatment, in the spirit of an expansion in the number of pairs involved. A perturbative analysis shows that in the high-frequency limit these processes are of higher order in  $1/\omega$ , and therefore do not contribute to the asymptotic behaviours of Eq. (8). In the intermediate-frequency regime one can ex-

pect the appearance of a  $n$ -plasmon threshold effect in the  $n$ -pair channel. Whereas at present we do not have a reliable quantitative estimate of the contribution of such processes to  $\text{Im}f_{xc}$ , we believe that their overall spectral strength will be a minor correction to the present results. This can be inferred from the good agreement between the two-pair result for  $K_{xc}$  and that from the Monte Carlo data, the difference being a quantitative measure of the integrated spectral strength of higher-order processes.

A different class of effects which could modify the present results are improved response functions in the two-pair channel, i.e. in Eq. (11). The main qualitative feature which is absent from all response functions that we have considered is plasmon damping. This will broaden the sharp feature present in 3D at the two-plasmon threshold. When the plasmon dispersion is positive (local-field-corrected results at small  $r_s$  and RPA) we expect small corrections, since the threshold behaviour is driven by the long-wavelength plasmon, whose linewidth vanishes as  $k^2$  for small  $k$ . In the case of negative plasmon dispersion, the collective excitation with minimum energy has nonzero wavevector and therefore non-vanishing linewidth due to decay into multiple particle-hole pairs. This indicates that the divergence in the two-pair spectrum found in the local-field-corrected results at large  $r_s$  (see Figures 6 and 8) is probably an artifact and would be replaced by a smooth peak if plasmon damping were included.

## V. SUMMARY

In this work we have given an extensive discussion of the exchange-correlation kernels  $f_{xc}^{L,T}(\omega)$ , both in 2 and in 3 spatial dimensions. We have presented an exact expression for the kernels in terms of four-point response functions, and evaluated it numerically within a non-perturbative approximate decoupling scheme, which accounts for two-pair processes. Our numerical results are qualitatively different from previously known interpolations. In 3D we predict a threshold behaviour, which can be understood as due to a simple phase-space effect, i.e. the opening of the two-plasmon channel in the two-pair spectrum. In 2D the same mechanism leads to a broad feature in the spectrum. We have also studied the influence of static-local-field corrections on our results and found even more marked deviations from previous theories.

We have obtained good agreement with all known asymptotic behaviours, including the newly-derived high-frequency limit of the transverse part and the Monte Carlo results for the bulk modulus. Estimates for the shear modulus and viscosity have also been given. Our results, which have been fitted to simple analytical formulas, provide the entire input necessary for non-adiabatic TD-DFT computations.

## ACKNOWLEDGMENTS

We wish to thank Prof. Giovanni Vignale, Dr. Carsten Ullrich and Dr. Helga M. Böhm for very useful discussions, and Dr. Lerwen Liu for sending us her data on  $G(k)$  in STLS in the two-dimensional case. One of us (RN) acknowledges the award of a short-term research grant by the FORUM/INFM Laboratory.

## APPENDIX A: TRANSVERSE RESPONSE FUNCTION FOR THE NON-INTERACTING FERMI GAS IN 2D AND 3D

The current-current response function for the non-interacting Fermi gas is given by

$$\chi_{ij}^0(\mathbf{k}, \omega) = \sum_{\mathbf{q}} \frac{\mathbf{q}^i \mathbf{q}^j}{m^2} \frac{n_{\mathbf{q}+\mathbf{k}/2}^F - n_{\mathbf{q}-\mathbf{k}/2}^F}{\omega - (\varepsilon_{\mathbf{q}-\mathbf{k}/2} - \varepsilon_{\mathbf{q}+\mathbf{k}/2}) + i\epsilon}, \quad (\text{A1})$$

where  $n_{\mathbf{q}}^F = 2\theta(k_F - |\mathbf{q}|)$  is the Fermi distribution function and  $\varepsilon_q = q^2/2m$  the free particle energy. It is sufficient to evaluate the transverse component of

$$A_{ij}(\mathbf{k}, \omega) = -\pi \int \frac{d^D q}{(2\pi)^D} n_q^F \frac{(\mathbf{q} + \frac{1}{2}\mathbf{k})^i}{m} \frac{(\mathbf{q} + \frac{1}{2}\mathbf{k})^j}{m} \times \delta(\omega + \varepsilon_{\mathbf{q}} - \varepsilon_{\mathbf{q}+\mathbf{k}}) \quad (\text{A2})$$

since  $\text{Im}\chi_{ij}^0(\mathbf{k}, \omega) = A_{ij}(\mathbf{k}, \omega) - A_{ij}(\mathbf{k}, -\omega)$ . Angular integration leads to

$$A^T(k, \omega) = -\frac{1}{\pi m k} \int_{m|\omega-\varepsilon_k|/k}^{k_F} dq \gamma_D q^D \theta(k_F - q) \quad (\text{A3})$$

where  $\gamma_2 = \sqrt{1-x^2}$ ,  $\gamma_3 = (1-x^2)/4$  and  $x = m|\omega - \varepsilon_k|/qk$ . It is convenient to work with the reduced variables  $z = k/2k_F$  and  $u = \omega m/kk_F$ . After integration we have

$$\text{Im}\chi_T^0(k, \omega) = l_D \frac{n}{mz} (B_+ - B_-) \quad (\text{A4})$$

with  $B_{\pm} = \theta(1 - |u \pm z|) [1 - (u \pm z)^2]^{\frac{D+1}{2}}$ ,  $l_3 = 3\pi/32$  and  $l_2 = 1/3$ .

The imaginary part of the ideal-gas transverse response function vanishes when  $|\omega| - 2kk_F/m > \varepsilon_k$ , as the longitudinal one. As a check of the present derivation we evaluate the third frequency moment sum rule, which leads to

$$M_T^0(k) = -\frac{2}{\pi} \int_0^\infty \omega \text{Im}\chi_T^0(k, \omega) d\omega = h_D \frac{n}{m} \varepsilon_k \varepsilon_F \quad (\text{A5})$$

with  $h_3 = 4/5$  and  $h_2 = 1$ , in agreement with (16) evaluated to zero order in the interaction potential  $v_k^L$ , i.e. with  $v_k^L = 0$ ,  $\langle ke \rangle = \frac{3}{5}\varepsilon_F$  in 3D and  $\langle ke \rangle = \frac{1}{2}\varepsilon_F$  in 2D.

The real part is obtained from the imaginary one via the Kramers-Kronig relation, which gives

$$\begin{aligned}\text{Re}\chi_T^0(k, \omega) &= \frac{3n}{8mz} \left[ z^3 + 3u^2z - \frac{5}{3}z \right. \\ &\quad \left. + \frac{1}{4}E_+^{(3)} - \frac{1}{4}E_-^{(3)} \right] \end{aligned}\quad (\text{A6})$$

with  $E_{\pm}^{(3)} = [(z \pm u)^2 - 1]^2 \ln \left| \frac{u \pm z - 1}{u \pm z + 1} \right|$  in 3D, and

$$\text{Re}\chi_T^0(k, \omega) = \frac{n}{3mz} \left[ 2z^3 + 6u^2z - 3z - E_+^{(2)} - E_-^{(2)} \right] \quad (\text{A7})$$

with  $E_{\pm}^{(2)} = [(z \pm u)^2 - 1]^{\frac{3}{2}} \theta(|z \pm u| - 1) \text{sgn}(z \pm u)$  in 2D.

We examine now some limiting behaviours. At long wavelength we get

$$\chi_T^0(k \rightarrow 0, \omega) = \frac{M_T^0(k)}{\omega^2} + g_D \frac{n}{m\omega^4} \varepsilon_k^2 \varepsilon_F^2, \quad (\text{A8})$$

where  $g_3 = 48/35$ ,  $g_2 = 1/2$  and  $M_T^0(k)$  as defined in (A5). At zero frequency we have instead

$$\begin{aligned}\chi_T^0(k, \omega = 0) &= -\frac{n}{m} \left[ \frac{5}{8} - \frac{3}{32} \frac{k^2}{k_F^2} \right. \\ &\quad \left. - \frac{3}{8} \frac{k_F}{k} \left( \frac{k^2}{4k_F^2} - 1 \right)^2 \ln \left| \frac{k - 2k_F}{k + 2k_F} \right| \right] \end{aligned}\quad (\text{A9})$$

in 3D, and

$$\begin{aligned}\chi_T^0(k, \omega = 0) &= -\frac{n}{m} \left[ 1 - \frac{k^2}{6k_F^2} \right. \\ &\quad \left. + \frac{4k_F}{3k} \left( \frac{k^2}{4k_F^2} - 1 \right)^{\frac{3}{2}} \theta(k - 2k_F) \right] \end{aligned}\quad (\text{A10})$$

in 2D. In both cases the  $\omega \rightarrow 0, k \rightarrow 0$  limit depends on the order in which the limits are taken, as in the longitudinal case.

## APPENDIX B: EVALUATION OF THE LOW- $k$ EXPANSION

In this Appendix we evaluate to leading order in  $k$  the second term in the RHS of Eq. (6), which obeys the equation of motion

$$\omega^2 \text{Im} \langle \langle [\mathbf{j}_k, H]; [\mathbf{j}_{-k}, H] \rangle \rangle_\omega = -\text{Im} \langle \langle [[\mathbf{j}_k, K + P], K + P]; [[\mathbf{j}_{-k}, K + P], K + P] \rangle \rangle_\omega, \quad (\text{B1})$$

where  $K$  and  $P$  denote the kinetic and potential terms of the Hamiltonian respectively. There are 16 terms in total, which correspond to the different combinations of  $K$  and  $P$ . Fortunately only 4 of them are relevant to our

calculations, as is shown in the following. Every commutator with  $K$  gives a factor of  $k$ , therefore terms containing more than two  $K$ 's do not contribute to leading order in  $k$ . The commutator  $[[\mathbf{j}_k, P], P]$  vanishes, since

$$[\mathbf{j}_k, P] = [\mathbf{j}_k, \sum_{\mathbf{q} \neq 0} v_q^L \rho_{\mathbf{q}} \rho_{-\mathbf{q}}] = -\frac{1}{V} \sum_{\mathbf{q} \neq 0} \frac{\mathbf{q}}{m} \rho_{\mathbf{q}+\mathbf{k}} \rho_{-\mathbf{q}} \quad (\text{B2})$$

and two density operators  $\rho_{\mathbf{q}}$  commute.

The remaining terms can be written as

$$\begin{aligned}-\frac{1}{\omega^2} \text{Im} \langle \langle [[\mathbf{j}_k, K], P] + [[\mathbf{j}_k, P], K]; \\ [[\mathbf{j}_{-k}, K], P] + [[\mathbf{j}_{-k}, P], K] \rangle \rangle_\omega. \end{aligned}\quad (\text{B3})$$

At this point we remark that the term  $P^{\text{res}} = V^{-1} v_k^L \rho_{\mathbf{k}} \rho_{-\mathbf{k}}$  of the Hamiltonian gives rise to a singular contribution to the equation of motion for  $\mathbf{j}_k$ ,

$$[\mathbf{k} \cdot \mathbf{j}_k, P^{\text{res}}] = \omega_{pi}^2 \rho_{\mathbf{k}} - \frac{k^2}{mV} v_k^L \rho_{2\mathbf{k}} \rho_{-\mathbf{k}}. \quad (\text{B4})$$

In the first term in the RHS the factor  $V^{-1}$  present in the others has been compensated by the factor  $\rho_0 = N$ . Therefore this term has to be treated separately when transforming the summations into integrals. We found it more convenient to replace the Hamiltonian  $H$  with  $\tilde{H} = H - P^{\text{res}}$  in the equation of motion for the response function, which allows to obtain the proper response function  $\tilde{\chi}$ . This can be easily understood from the diagrammatic definition of  $\tilde{\chi}$  as the sum of all diagrams that cannot be split by cutting a single interaction line: this necessarily carries a factor  $v_{\mathbf{q}=\mathbf{k}}^L$ , which has been excluded from  $\tilde{H}$ . Using  $\tilde{H}$  one also excludes all non-singular contributions having a factor  $v_{\mathbf{q}=\mathbf{k}}^L$ , as for example the second term in the RHS of (B4). These terms however contain a factor  $V^{-1}$  and are irrelevant in the thermodynamic limit.

All considerations made previously hold with the new Hamiltonian, provided that we are computing the proper current-current response in Eq. (6). The commutators in (B3) are given by

$$\begin{aligned}[[\mathbf{j}_k^i, K], P] &= -\frac{1}{mV} \sum_{\mathbf{q}} v_q^L \left( \frac{\mathbf{q}^i}{m} \mathbf{k}^l + \mathbf{q} \cdot \mathbf{k} \delta_{il} \right) \mathbf{j}_{\mathbf{q}+\mathbf{k}}^l \rho_{-\mathbf{q}}, \\ [[\mathbf{j}_k^i, P], K] &= \frac{1}{mV} \sum_{\mathbf{q}} \left[ v_{|\mathbf{q}+\mathbf{k}|}^L (\mathbf{q} + \mathbf{k})^i - v_q^L \mathbf{q}^i \right] \\ &\quad \times (\mathbf{q} + \mathbf{k}) \cdot \mathbf{j}_{\mathbf{q}+\mathbf{k}} \rho_{-\mathbf{q}}. \end{aligned}\quad (\text{B5})$$

where terms containing a single  $\rho_{\mathbf{k}}$  operator have been neglected for reasons explained below. From Eqs. (6), (B3) and (B5) we get

$$\begin{aligned}\text{Im} \tilde{\chi}_{ij}(\mathbf{k}, \omega) &= \frac{1}{m^2 V^2 \omega^4} \sum_{\mathbf{q} \mathbf{q}'} \text{Im} \langle \langle \mathbf{j}_{\mathbf{q}+\mathbf{k}}^i \rho_{-\mathbf{q}}; \mathbf{j}_{\mathbf{q}'-\mathbf{k}}^{j'} \rho_{-\mathbf{q}'} \rangle \rangle_\omega \\ &\quad \times \Gamma^{il}(\mathbf{q}, \mathbf{k}) \Gamma^{jl'}(\mathbf{q}', -\mathbf{k}) + o(k^2) \end{aligned}\quad (\text{B6})$$

where  $\Gamma$  is given by

$$\begin{aligned}\Gamma^{il}(\mathbf{q}, \mathbf{k}) &= \left( v_{|\mathbf{q}+\mathbf{k}|}^L - v_q^L \right) \mathbf{q}^i \mathbf{q}^l \\ &\quad + v_q^L (\mathbf{q}^l \mathbf{k}^i - \mathbf{k}^l \mathbf{q}^i - \delta_{il} \mathbf{q} \cdot \mathbf{k}).\end{aligned}\quad (\text{B7})$$

We remark that (B6) is valid for every Fourier-trasformable interparticle potential, and is not restricted to  $T = 0$ .

The tensor  $\Gamma$  is of first order in  $k$  and the product of the two tensors in (B6) is of second order, so that in the response function we can safely set  $\mathbf{k} = 0$ , leading to Eq. (7). This also explains why terms containing one  $\rho_{\mathbf{k}}$  have been neglected in the commutators (B5):  $\rho_0$  is constant in time and its commutator with  $\mathbf{j}_{\mathbf{q}} \rho_{-\mathbf{q}}$  vanishes.

### APPENDIX C: EVALUATION OF THE HIGH-FREQUENCY LIMIT VIA PERTURBATIVE EXPANSION

Starting from Eq. (7) we evaluate the high frequency limit of  $f_{xc}(\omega)$  to second order in perturbation theory. In this way we extend to the transverse case the results obtained by Glick and Long<sup>25</sup> in 3D and by Holas and Singwi<sup>37</sup> in 2D on the asymptotic behaviour of  $f_{xc}$ . The discussion will also clarify the nature of the exchange processes which we approximately included in the decoupling (11) via the factor  $g_x$  of Eq. (10).

The four-point response function can be written as

$$\begin{aligned}\text{Im} \langle\langle \mathbf{j}_{\mathbf{q}}^l \rho_{-\mathbf{q}}; \mathbf{j}_{\mathbf{q}'}^{l'} \rho_{-\mathbf{q}'} \rangle\rangle_{\omega} &= \\ &= -\pi \sum_{\mathbf{p}_1 \mathbf{p}_2 \mathbf{p}_3 \mathbf{p}_4} \frac{\left( \mathbf{p}_1 + \frac{\mathbf{q}}{2} \right)^l \left( \mathbf{p}_2 - \frac{\mathbf{q}'}{2} \right)^{l'}}{m^2} \\ &\quad \times \sum_n \delta(\omega n_0 - \omega) \langle 0 | c_{\mathbf{p}_1}^+ c_{\mathbf{p}_3}^+ c_{\mathbf{p}_1 + \mathbf{q}} c_{\mathbf{p}_3 - \mathbf{q}} | n \rangle \\ &\quad \times \langle n | c_{\mathbf{p}_2 - \mathbf{q}'}^+ c_{\mathbf{p}_4 + \mathbf{q}'}^+ c_{\mathbf{p}_2} c_{\mathbf{p}_4} | 0 \rangle\end{aligned}\quad (\text{C1})$$

where  $|0\rangle$  and  $|n\rangle$  denote the exact eigenstates of the system, and the spin index is implicit. Since each  $\Gamma$  in (B6) contains a factor  $v_q^L$ , we can evaluate the four-point response function at zero order in perturbation theory, *i.e.* for the non-interacting electron gas, so that  $\omega_{n0} = (\mathbf{q}'^2/m) + (\mathbf{p}_4 - \mathbf{p}_3) \cdot \mathbf{q}'/m$ .

The product of expectation values in the previous equation is different from zero only when  $p_1, p_2, p_3, p_4 < k_F$ , which in the high-frequency limit implies  $p_i \ll q \simeq q' \simeq \sqrt{m\omega}$ . These considerations allow us to simplify (C1) as

$$\begin{aligned}\text{Im} \langle\langle \mathbf{j}_{\mathbf{q}}^l \rho_{-\mathbf{q}}; \mathbf{j}_{\mathbf{q}'}^{l'} \rho_{-\mathbf{q}'} \rangle\rangle_{\omega \rightarrow \infty} &= \pi \frac{\mathbf{q}^l \mathbf{q}^{l'}}{4m^2} \delta \left( \frac{q'^2}{m} - \omega \right) \\ &\times \sum_{\mathbf{p}_1 \mathbf{p}_2 \mathbf{p}_3 \mathbf{p}_4} \langle 0 | c_{\mathbf{p}_1}^+ c_{\mathbf{p}_3}^+ c_{\mathbf{p}_1 + \mathbf{q}} c_{\mathbf{p}_3 - \mathbf{q}} c_{\mathbf{p}_2 - \mathbf{q}'}^+ c_{\mathbf{p}_4 + \mathbf{q}'}^+ c_{\mathbf{p}_2} c_{\mathbf{p}_4} | 0 \rangle\end{aligned}\quad (\text{C2})$$

With  $a, b, g, h < k_F$  and  $c, d, e, f > k_F$ , we have

$$\begin{aligned}\langle 0 | c_a^+ c_b^+ c_c c_d c_e^+ c_f^+ c_g c_h | 0 \rangle &= (\delta_{a,h} \delta_{b,g} - \delta_{a,g} \delta_{b,h}) \\ &\quad \times (\delta_{d,e} \delta_{c,f} - \delta_{c,e} \delta_{d,f}).\end{aligned}\quad (\text{C3})$$

There are 4 terms overall, two of which are negative because of the anticommutation rules and mix together field operators belonging to different density (or current density) operators. These terms, which we call exchange terms, are neglected in the decoupling (9) and carry an overall factor  $-\frac{1}{2}$  due to spin (see below). The first term  $\delta_{a,h} \delta_{b,g} \delta_{d,e} \delta_{c,f}$  imposes the following constraints on the wave vectors and spin indices,

$$\begin{aligned}\mathbf{p}_1 &= \mathbf{p}_4 \quad \sigma_1 = \sigma_4 \quad \mathbf{p}_1 + \mathbf{q} = \mathbf{p}_4 + \mathbf{q}' \quad \sigma_1 = \sigma_4, \\ \mathbf{p}_2 &= \mathbf{p}_3 \quad \sigma_2 = \sigma_3 \quad \mathbf{p}_3 - \mathbf{q} = \mathbf{p}_2 - \mathbf{q}' \quad \sigma_2 = \sigma_3.\end{aligned}\quad (\text{C4})$$

The sum is done on  $\mathbf{p}_1, \sigma_1$   $\mathbf{p}_2, \sigma_2$ , and brings a factor  $N^2 \delta_{\mathbf{q}, \mathbf{q}'}$ , with  $N$  the number of particles. The second term  $\delta_{a,g} \delta_{b,h} \delta_{d,e} \delta_{c,f}$  gives

$$\begin{aligned}\mathbf{p}_1 &= \mathbf{p}_3 \quad \sigma_1 = \sigma_3 \quad \mathbf{p}_1 + \mathbf{q} = \mathbf{p}_4 + \mathbf{q}' \quad \sigma_2 = \sigma_4, \\ \mathbf{p}_2 &= \mathbf{p}_4 \quad \sigma_1 = \sigma_4 \quad \mathbf{p}_3 - \mathbf{q} = \mathbf{p}_2 - \mathbf{q}' \quad \sigma_2 = \sigma_3.\end{aligned}\quad (\text{C5})$$

Unlike the first one, this second term fixes all the four  $\sigma$ 's, contributing with a factor  $-\frac{N^2}{2} \delta_{\mathbf{q}, -\mathbf{q}'}$  which is half the opposite of the first one.

The remaining two terms are obtained in an analogous way, and their overall contribution is also  $\frac{N^2}{2} \delta_{\mathbf{q}, -\mathbf{q}'}$ . Putting all terms together we get

$$\begin{aligned}\text{Im} \langle\langle \mathbf{j}_{\mathbf{q}}^l \rho_{-\mathbf{q}}; \mathbf{j}_{\mathbf{q}'}^{l'} \rho_{-\mathbf{q}'} \rangle\rangle_{\omega \rightarrow \infty} &= \frac{\pi N^2}{2 m^2} (\delta_{\mathbf{q}, \mathbf{q}'} + \delta_{-\mathbf{q}, \mathbf{q}'}) \\ &\quad \times \frac{\mathbf{q}^l \mathbf{q}^{l'}}{4} \delta \left( \frac{q^2}{m} - \omega \right).\end{aligned}\quad (\text{C6})$$

Substitution of the previous expression in Eq. (7) and small  $k$  expansion lead to Eq. (8).

An estimate of higher-order corrections can be obtained from additional applications of the equation of motion for  $\mathbf{j}_{\mathbf{q}}$ . Third-order perturbation theory treats one of the two pairs to first order and is irrelevant for large  $q$  and  $\omega$ . To fourth order in  $v_k^L$ , one obtains instead three-pair contributions which contain two additional commutators with  $P$  in the last term of Eq. (6). Considering that the transferred momentum scales as  $\sqrt{\omega}$  at large  $\omega$ , these scale as  $\omega^{-1-D}$  and therefore do not affect the leading behaviour given by second-order perturbative expansion.

---

\* Present address: Max-Planck-Institute for Mathematics in the Sciences, D-04103 Leipzig, Germany.

<sup>1</sup> A. vom Felde, J. Sprösser-Prou, and J. Fink, Phys. Rev. B **40**, 10181 (1989).

<sup>2</sup> B. C. Larson, J. Z. Tishler, E. D. Isaacs, P. Zschack, A. Fleszar, and A. G. Eguiluz, Phys. Rev. Lett. **77**, 1346 (1996).

<sup>3</sup> E. Runge and E. K. U. Gross, Phys. Rev. Lett. **52**, 997 (1984).

<sup>4</sup> E. K. U. Gross, J. F. Dobson, and M. Petersilka, in *Density Functional Theory, Topics in Current Chemistry*, edited by R. F. Nalewajski (Springer, Berlin, 1996).

<sup>5</sup> A. Zangwill and P. Soven, Phys. Rev. Lett. **45**, 204 (1980).

<sup>6</sup> A. Zangwill and P. Soven, Phys. Rev. B **24**, 4121 (1981).

<sup>7</sup> W. Ekardt, Phys. Rev. Lett. **52**, 1925 (1984).

<sup>8</sup> W. Ekardt, Phys. Rev. B **31**, 6360 (1985).

<sup>9</sup> E. K. U. Gross and W. Kohn, Phys. Rev. Lett. **55**, 2850 (1985); erratum in Phys. Rev. Lett. **57**, 923 (1986).

<sup>10</sup> N. Iwamoto and E. K. U. Gross, Phys. Rev. B **35**, 3003 (1987).

<sup>11</sup> J. Dobson, Phys. Rev. Lett. **73**, 2244 (1994).

<sup>12</sup> J. Dobson, in *Density Functional Theory, NATO ASI*, edited by E. K. U. Gross and R. M. Dreizler (Plenum, New York, 1994), p. 393.

<sup>13</sup> G. Vignale, Phys. Rev. Lett. **74**, 3233 (1995).

<sup>14</sup> G. Vignale, Phys. Lett. A **209**, 206 (1995).

<sup>15</sup> G. Vignale and W. Kohn, Phys. Rev. Lett. **77**, 2037 (1996).

<sup>16</sup> G. Vignale and W. Kohn, in *Electronic Density Functional Theory*, edited by J. Dobson, M. P. Das, and G. Vignale (Plenum Press, New York, 1997).

<sup>17</sup> G. Vignale, C. A. Ullrich, and S. Conti, Phys. Rev. Lett. **79**, 4878 (1997).

<sup>18</sup> C. A. Ullrich and G. Vignale, to be published (1998).

<sup>19</sup> B. Dabrowski, Phys. Rev. B **34**, 4989 (1986).

<sup>20</sup> H. M. Böhm, S. Conti, and M. P. Tosi, J. Phys.: Condens. Matter **8**, 781 (1996).

<sup>21</sup> D. F. DuBois, Ann. Phys. (NY) **8**, 24 (1959).

<sup>22</sup> D. F. DuBois and M. G. Kivelson, Phys. Rev. B **186**, 409 (1969).

<sup>23</sup> B. W. Ninham, C. J. Powell, and N. Swanson, Phys. Rev. **145**, 209 (1966).

<sup>24</sup> M. Hasegawa and M. Watabe, J. Phys. Soc. Jpn. **27**, 1393 (1969).

<sup>25</sup> A. J. Glick and W. F. Long, Phys. Rev. B **4**, 3455 (1971).

<sup>26</sup> W. Gasser, Zs. Phys. B **57**, 15 (1984).

<sup>27</sup> W. Gasser, Physica B **183**, 217 (1992).

<sup>28</sup> M. E. Bachlechner, W. Macke, H. M. Miesenböck, and A. Schinner, Physica B **168**, 104 (1991).

<sup>29</sup> M. E. Bachlechner, H. M. Böhm, and A. Schinner, Phys. Lett. A **178**, 186 (1993).

<sup>30</sup> D. Neilson, L. Swierkowski, A. Sjölander, and J. Szymanowski, Phys. Rev. B **44**, 6291 (1991).

<sup>31</sup> S. Conti, R. Nifosi, and M. P. Tosi, J. Phys.: Condens. Matter **9**, L475 (1997).

<sup>32</sup> R. Nifosi, S. Conti, and M. P. Tosi, Physica E **1**, 188 (1998).

<sup>33</sup> D. Pines and P. Nozières, *The Theory of Quantum Liquids* (Benjamin, New York, 1966), Vol. 1.

<sup>34</sup> K. S. Singwi and M. P. Tosi, in *Solid State Physics*, edited by H. Ehrenreich, F. Seitz, and D. Turnbull (Academic, New York, 1981), Vol. 36, p. 177.

<sup>35</sup> J. Lindhard, Mat.-Fys. Medd.-K. Dan. Vidensk. Selsk. **28**, No. 8 (1954).

<sup>36</sup> F. Stern, Phys. Rev. Lett. **18**, 546 (1967).

<sup>37</sup> A. Holas and K. S. Singwi, Phys. Rev. B **40**, 158 (1989).

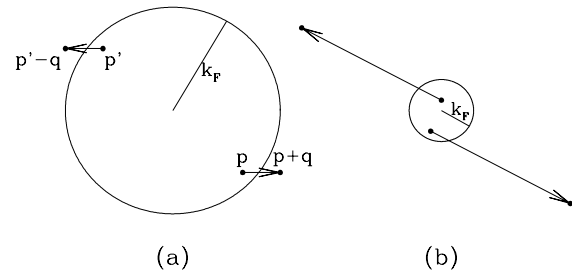


FIG. 1. Structure of two-pair excitations in a Fermi liquid for energies much smaller (a) and much bigger (b) than the Fermi energy. The arrows join the electron and hole of each pair, their length is the transferred wavevector  $\mathbf{q}$ .

<sup>38</sup> If the screened potential  $\tilde{v}_k^L$  is considered, the ratio  $\tilde{v}_{k_F}^L/\tilde{v}_q^L$  is still small at high density (i.e. large  $k_F$ ). At low density, on the other hand, the region  $q \ll k_F$  (i.e.  $\omega \ll \varepsilon_F$ ) shrinks to zero.

<sup>39</sup> L. D. Landau and E. Lifshitz, *Mechanics of Fluids*, Vol. 6 of *Course of Theoretical Physics*, 2nd ed. (Pergamon Press, Oxford, 1987).

<sup>40</sup> D. M. Ceperley and B. J. Alder, Phys. Rev. Lett. **45**, 566 (1980).

<sup>41</sup> S. H. Vosko, L. Wilk, and M. Nusair, Can. J. Phys. **58**, 1200 (1980).

<sup>42</sup> F. Rapisarda and G. Senatore, Aust. J. Phys. **49**, 161 (1996).

<sup>43</sup> L. D. Landau and E. Lifshitz, *Theory of Elasticity*, Vol. 7 of *Course of theoretical Physics*, 3rd ed. (Pergamon Press, Oxford, 1986).

<sup>44</sup> If complete consistency with  $K_{xc}^{\text{MC}}$  is desired, one simple possibility would be to multiply  $\text{Im}f_{xc}^{L,T}(\omega)$  by a constant  $\beta$ , chosen so as to satisfy  $K_{xc} = K_{xc}^{\text{MC}}$ , i.e.

$$\beta = \frac{K_{xc}^{\text{MC}} - n^2 [f_{xc}^L(\infty) - 2\frac{D-1}{D} f_{xc}^T(\infty)]}{K_{xc} - n^2 [f_{xc}^L(\infty) - 2\frac{D-1}{D} f_{xc}^T(\infty)]}.$$

<sup>45</sup> K. S. Singwi, M. P. Tosi, R. H. Land, and A. Sjölander, Phys. Rev. **176**, 589 (1968).

<sup>46</sup> P. Vashishta and K. S. Singwi, Phys. Rev. B **6**, 875 (1972).

<sup>47</sup> M. Jonson, J. Phys. C **9**, 3055 (1976).

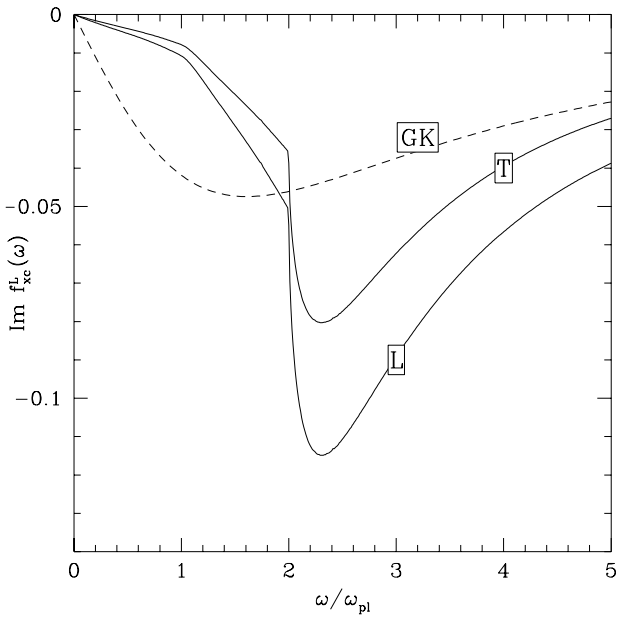


FIG. 2. Imaginary part of  $f_{xc}^{L,T}(\omega)$  in 3D at  $r_s = 3$  in units of  $2\omega_{pl}/n$ , as functions of  $\omega/\omega_{pl}$ . The dashed line gives the Gross-Kohn<sup>9,10</sup> interpolation scheme.

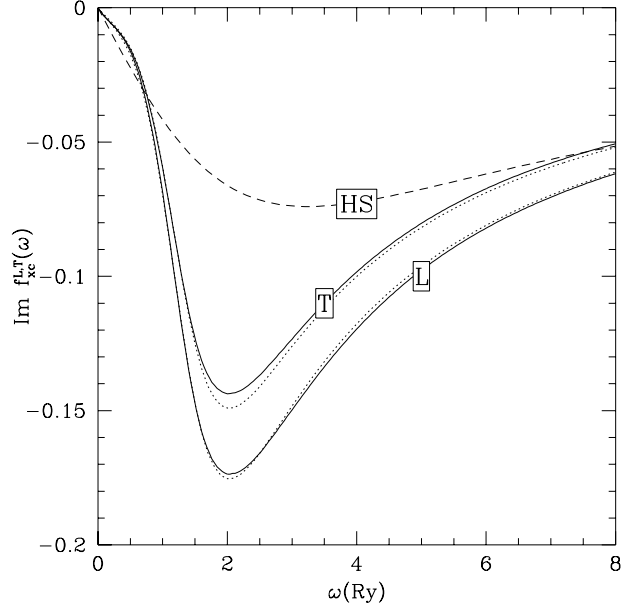


FIG. 4. Imaginary part of  $f_{xc}^{L,T}(\omega)$  in 2D at  $r_s = 3$  in units of  $Ry/n$ , as functions of  $\omega$  (in Ry). The dashed line gives the Holas-Singwi<sup>37</sup> interpolation and the dotted lines are the fit discussed in the text.

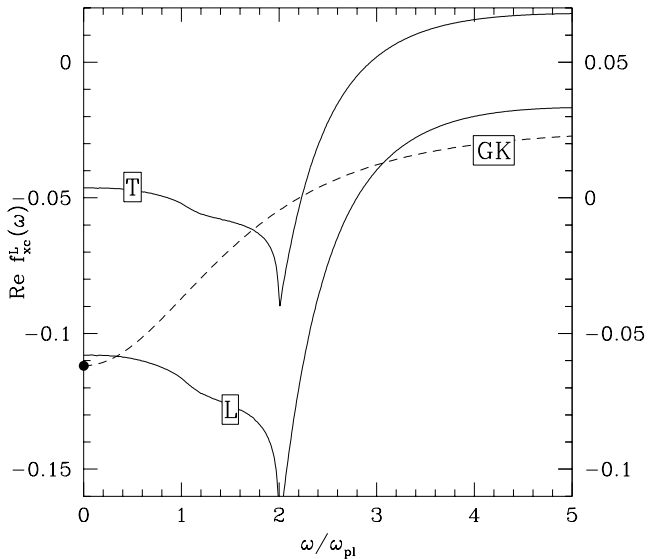


FIG. 3. Real part of  $f_{xc}^{L,T}(\omega)$  in 3D at  $r_s = 3$ . Notations and units are as in Fig. 2. The dot on the left axis marks  $K_{xc}^{MC}/n^2$ . The scale for the transverse component is on the right-hand axis.

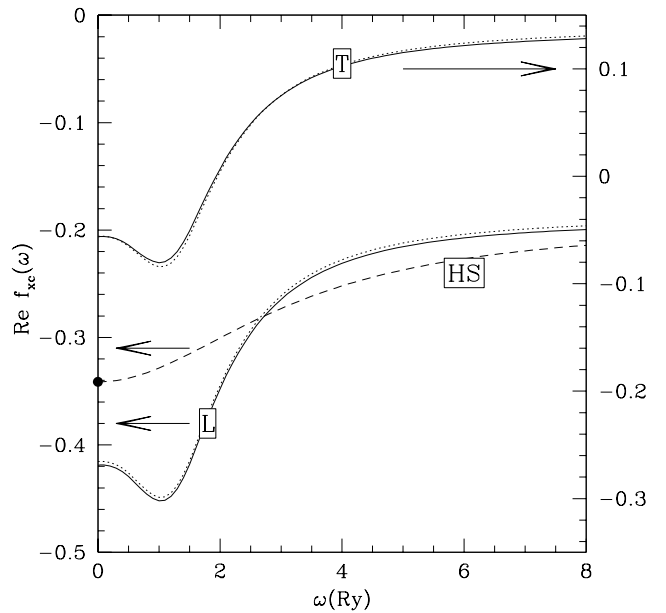


FIG. 5. Real part of  $f_{xc}^{L,T}(\omega)$  in 2D at  $r_s = 3$  in units of  $Ry/n$ , as functions of  $\omega$  (in Ry), the scale for the transverse component being on the right-hand axis. The dashed line gives the Holas-Singwi<sup>37</sup> interpolation and the dotted lines show the fit discussed in the text. The dot on the left axis marks  $K_{xc}^{MC}/n^2$ .

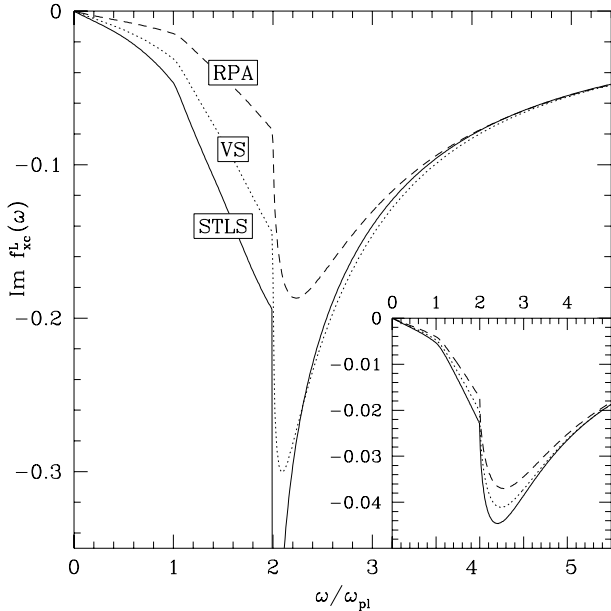


FIG. 6. Imaginary part of  $f_{xc}^L(\omega)$  in 3D in units of  $2\omega_{pl}/n$ , as a function of  $\omega/\omega_{pl}$  at  $r_s = 5$  (main figure) and  $r_s = 1$  (inset). We plot results obtained using RPA response functions (dashed curve), STLS response functions (full curve) and VS response functions (dotted curve).

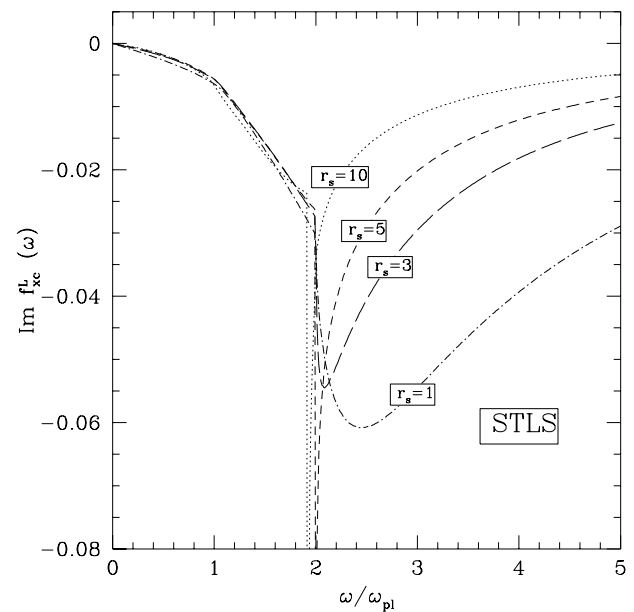


FIG. 8. Imaginary part of  $f_{xc}^L(\omega)$  in 3D, in units of  $2r_s^{-3/2}\omega_{pl}/n$ , computed with STLS response functions, at various values of  $r_s$ .

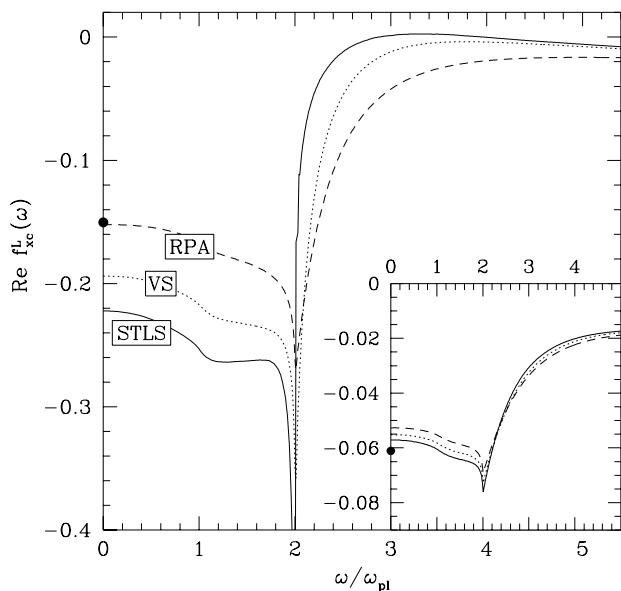


FIG. 7. Real part of  $f_{xc}^L(\omega)$  in 3D in units of  $2\omega_{pl}/n$ , as a function of  $\omega/\omega_{pl}$  at  $r_s = 5$  (main figure) and  $r_s = 1$  (inset). We plot results obtained using RPA response functions (dashed curve), STLS response functions (full curve) and VS response functions (dotted curve). The dots mark  $K_{xc}^{MC}/n^2$ .

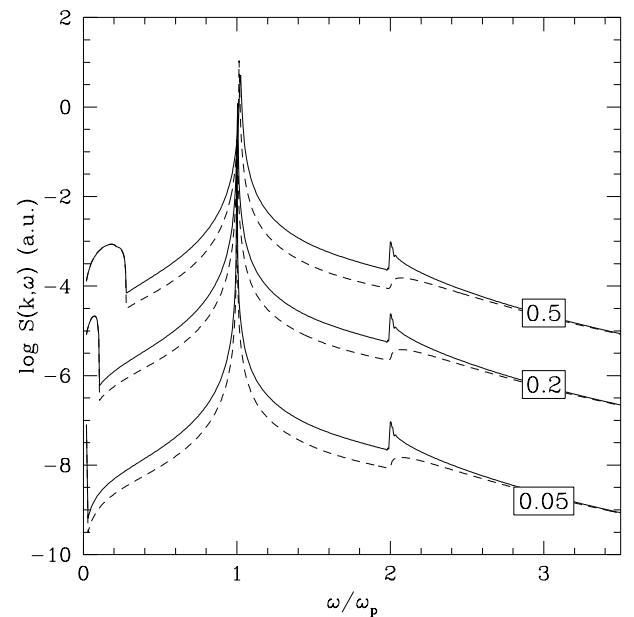


FIG. 9. Dynamic structure factor  $S(k, \omega)$  at  $r_s = 5$  as a function of  $\omega/\omega_{pl}$  shown in the flags on a semilogarithmic scale at various values of  $kr_s a_B$ , as obtained from STLS (full curves) and RPA (dashed curves) calculations.

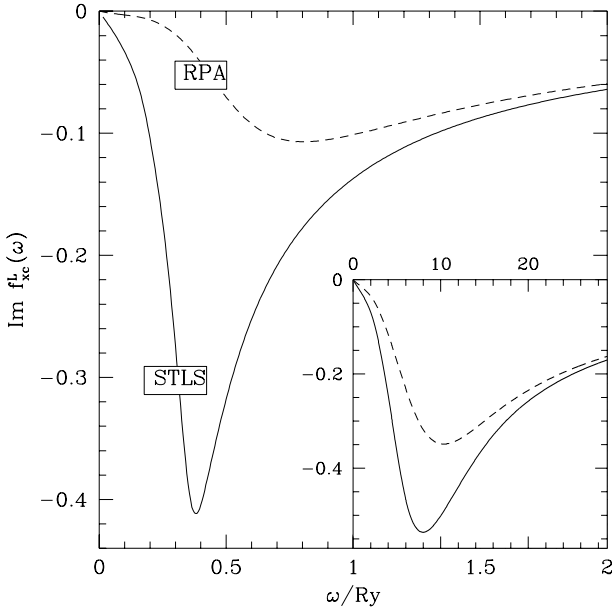


FIG. 10. Imaginary part of  $f_{xc}^L(\omega)$  in 2D in units of  $Ry/n$ , as a function of  $\omega$  (in  $Ry$ ) at  $r_s = 6$  (main figure) and  $r_s = 1$  (inset). We plot results obtained using RPA response functions (dashed curves) and STLS response functions (full curves).

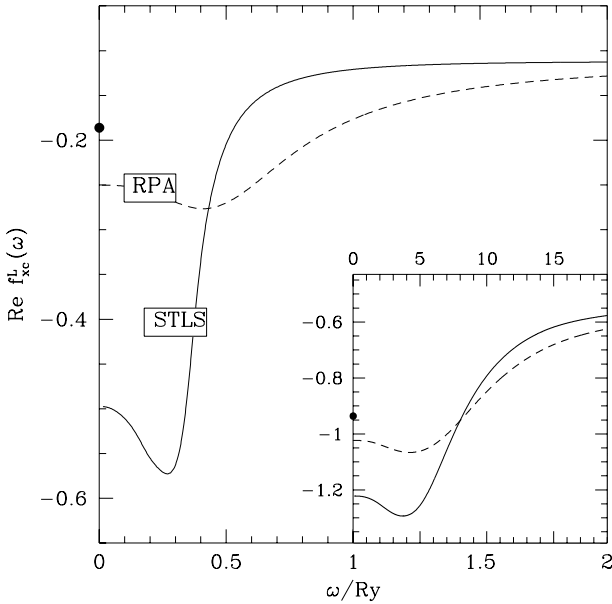


FIG. 11. Real part of  $f_{xc}^L(\omega)$  in 2D in units of  $Ry/n$ , as a function of  $\omega$  (in  $Ry$ ) at  $r_s = 6$  (main figure) and  $r_s = 1$  (inset). We plot results obtained using RPA response functions (dashed curve) and STLS response functions (full curves). The dots mark  $K_{xc}^{MC}/n^2$ .

TABLE I. Exact high- $\omega$  limits of  $f_{xc}^{L,T}(\omega)$  in 3D and bulk modulus  $K_{xc}^{\text{MC}}$  obtained from the Monte Carlo equation of state; shear viscosity  $\eta$  and shear and bulk moduli ( $\mu_{xc}$  and  $K_{xc}$ ) obtained from the RPA treatment of two pair processes.  $f_{xc}$  is in units of  $2\omega_{pl}/n$ ,  $\eta$  in units of  $n$ ,  $K_{xc}$  and  $\mu_{xc}$  in units of  $2\omega_{pl}n$ . Values in atomic units ( $a_B = m = e^2 = 1$ ) can be obtained from  $\eta^{AU} = 3/(4\pi r_s^3)\eta^{\text{tab}}$ ,  $(K, \mu)^{AU} = 3^{3/2}r_s^{-9/2}/(2\pi)(K, \mu)^{\text{tab}}$ , where <sup>tab</sup> denotes the tabulated values. The last reported decimal figure is likely to be affected by numerical inaccuracies.

$r_s$	$K_{xc}^{\text{MC}}$	$f_{xc}^L(\infty)$	$f_{xc}^T(\infty)$	$\eta$	$\mu_{xc}$	$K_{xc}$
0.5	-0.04246	-0.01794	0.0177	0.0029	0.0065	-0.0425
1	-0.0611	-0.0216	0.0284	0.0062	0.0064	-0.0612
2	-0.0891	-0.0252	0.0457	0.012	0.0052	-0.0896
3	-0.1119	-0.0280	0.0600	0.017	0.0037	-0.1128
4	-0.1320	-0.0308	0.0724	0.021	0.0020	-0.1335
5	-0.1503	-0.0338	0.0835	0.024	0.0002	-0.1525
6	-0.1674	-0.0370	0.0935	0.027	-0.0018	-0.1702
10	-0.2276	-0.0518	0.1267	0.034	-0.010	-0.233
15	-0.2917	-0.0725	0.1587	0.040	-0.023	-0.301
20	-0.3483	-0.0939	0.1847	0.044	-0.036	-0.361

TABLE II. Exact high- $\omega$  limits of  $f_{xc}^{L,T}(k, \omega)$  in 2D and bulk modulus  $K_{xc}^{\text{MC}}$  obtained from the Monte Carlo equation of state; shear viscosity  $\eta$  and shear and bulk moduli ( $\mu_{xc}$  and  $K_{xc}$ ) obtained from the RPA treatment of two-pair processes.  $f_{xc}$  is in units of  $Ry/n$ ,  $\eta$  in units of  $n$ ,  $K_{xc}$  and  $\mu_{xc}$  in units of  $Ry \cdot n$ . Values in atomic units can be obtained from  $\eta^{AU} = 1/(\pi r_s^2)\eta^{\text{tab}}$ ,  $(K, \mu)^{AU} = 1/(2\pi r_s^2)(K, \mu)^{\text{tab}}$ , where <sup>tab</sup> denotes the tabulated values. The last reported decimal figure is likely to be affected by numerical inaccuracies.

$r_s$	$K_{xc}^{\text{MC}}$	$f_{xc}^L(\infty)$	$f_{xc}^T(\infty)$	$\eta$	$\mu_{xc}$	$K_{xc}$
1	-0.9360	-0.5499	0.3372	0.018	-0.064	-0.959
2	-0.4912	-0.2750	0.1916	0.029	-0.064	-0.514
3	-0.3413	-0.1933	0.1330	0.035	-0.058	-0.363
4	-0.2649	-0.1535	0.1010	0.040	-0.054	-0.285
5	-0.2180	-0.1294	0.0810	0.043	-0.050	-0.236
6	-0.1860	-0.1128	0.067	0.045	-0.047	-0.203
10	-0.1191	-0.0768	0.0395	0.050	-0.039	-0.132
15	-0.0833	-0.0560	0.0257	0.052	-0.033	-0.094
20	-0.0645	-0.0445	0.0189	0.054	-0.028	-0.073

TABLE III. Interpolation parameters according to Eq. (22), in 2D. The last reported decimal figure is likely to be affected by numerical inaccuracies.

$r_s$	$10^{-3} c_0 r_s^{5/2}$	$c_1 r_s^2$	$c_2$	$c_3$	$c_4$
1	62.7	1.10	9.94	37.4	6.84
2	2.90	59.2	-1.74	4.62	7.70
3	1.73	34.9	-3.79	12.5	15.1
4	1.44	28.6	-3.45	15.8	30.3
5	1.18	22.5	-2.64	16.3	47.9
6	0.943	17.3	-2.04	15.8	66.2
10	0.458	7.23	-1.0	13.1	150
15	0.250	3.42	-0.524	10.9	276
20	0.160	1.96	-0.313	9.52	430